ROYAL SOCIETY
OF CHEMISTRY

PAPER

Check for updates

Luminescent Cd(II)–organic frameworks with chelating NH₂ sites for selective detection of Fe(III) and antibiotics†

Dan Zhao,[a] Xiao-Hui Liu,[a] Yue Zhao,[a] Peng Wang,[a] Yi Liu,[a] Mohammad Azam,[b] Saud I. Al-Resayes,[b] Yi Lu*[a] and Wei-Yin Sun [iD] *[a]

Excess and deficiency of iron(III) and antibiotics from normal permissible limits will induce serious disorders, so their detection is important but challenging. In this work, by introducing a new amino triazole ligand N^1-(4-(1H-1,2,4-triazole-1-yl)benzyl)-N^1-(2-aminoethyl)ethane-1,2-diamine (L), a series of Cd(II)-based metal–organic frameworks (MOFs) $[Cd_3(BDC)_3(DMF)_2]$ (**1**), $[Cd(L)(BDC)]_2 \cdot 2DMF \cdot H_2O$ (**2**), $[NaCd_2(L)(BDC)_{2.5}] \cdot 9H_2O$ (**3**), $[Cd_2(L)(2,6\text{-}NDC)_2] \cdot DMF \cdot 5H_2O$ (**4**) and $[Cd_2(L)(BPDC)_2] \cdot DMF \cdot 9H_2O$ (**5**) were synthesized. MOFs **1**, **2** and **3** obtained under the same conditions with the same auxiliary ligand (H_2BDC) but different amounts of alkali (NaOH) show distinct 3D, 1D and 3D framework structures, respectively, in which L and BDC^{2-} exhibit varied coordination modes. **4** and **5** with 3D structures were isolated by using longer auxiliary ligands of 2,6-H_2NDC and H_2BPDC. The porosity and excellent fluorescence performance of **3**, **4** and **5** make them potential luminescent sensors for Fe(III) and antibiotics. The results show that **3**, **4** and **5** represent high sensitivity for the detection of Fe(III) ions with detection limits of 155 ppb for **3**, 209 ppb for **4** and 297 ppb for **5** due to the existence of open channels and chelating NH₂ sites. In addition, the strong emissions of **3**, **4** and **5** can be quenched efficiently by trace amounts of NFs (nitrofurazone, NZF; nitrofurantoin, NFT; furazolidone, FZD) antibiotics even in the presence of other competing antibiotics such as β-lactams (penicillin, PCL). They are responsive to NZF with detection limits of 162 ppb for **3**, 75 ppb for **4** and 60 ppb for **5**.

1. Introduction

Iron, one of the most important and indispensable elements in metabolic processes, is extensively distributed in environmental and biological systems.[1] Both shortage and surplus of iron may result in disorders such as skin diseases, iron deficiency anemia (IDA), agrypnia and decreased immunity.[2] In this regard, selective and sensitive detection of trace amounts of iron ions has practical significance.[3–9] Similarly, antibiotics, as a treatment of bacterial infections, are widely used in aquacultures and the abuse of them has led to high levels of antibiotic residues.[10] Antibiotics have been recognized as a class of serious organic pollutants because of their high toxicity and difficulty in

degradation by nature.[11] Thus, monitoring and removing such specific pollutants are important, but challenging.[12]

Very recently, luminescent metal–organic frameworks (MOFs) are of bright promise as a new type of sensing material because of their prominent optical properties, permanent porosity, tunable structure and relatively long emission wavelength.[13–15] To date, chemists have synthesized various luminescent MOF-based probes for application in the detection of metal ions, explosives, small molecules, *etc.*[16–24] To obtain an effective MOF sensor, a binding site, powerful luminophore and stable architecture are required. An effective strategy to synthesize luminescent MOF-based probes is to use chelating agents (receptor units) to produce a distinct fluorescence upon chelation by interacting with the target metal ion (analyte) selectively and efficiently.[25,26] Once the analyte is recognized by the receptor, the fluorescence signals can be observed in the form of quenching or enhancement in the fluorescence due to either electron transfer (eT), charge transfer (CT), or energy transfer (ET) processes.[27] To date, chelating agents with functional groups, such as pyridyl, amide and hydroxyl groups, have been immobilized in luminescent MOFs.[28–32] Particularly, the NH₂ group in organic luminescent materials can be regarded as an electron-donating group suitable for binding the electron-accepting metal ions.

[a]Coordination Chemistry Institute, State Key Laboratory of Coordination Chemistry, School of Chemistry and Chemical Engineering, Nanjing National Laboratory of Microstructures, Collaborative Innovation Center of Advanced Microstructures, Nanjing University, Nanjing 210023, China. E-mail: luyi@nju.edu.cn; sunwy@nju.edu.cn; Tel: +86 25 89683485

[b]Department of Chemistry, College of Science, King Saud University, P. O. Box 2455, Riyadh 11451, Kingdom of Saudi Arabia

† Electronic supplementary information (ESI) available: X-ray crystallographic data in CIF format, IR spectra, structural illustrations, TG and PXRD, detection of antibiotics. CCDC 1547776–1547780. For ESI and crystallographic data in CIF or other electronic format see DOI: 10.1039/c7ta03849f
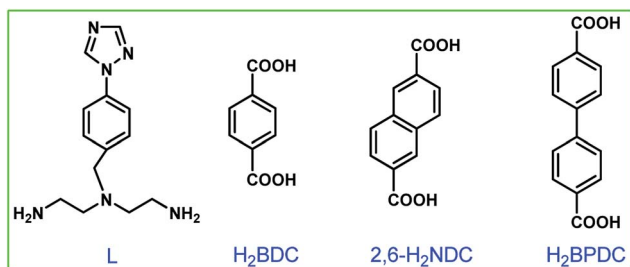
Scheme 1 Structures of ligands L, H$_2$BDC, 2,6-H$_2$NDC and H$_2$BPDC.

Based on the consideration mentioned above, we prepared a new amino triazole ligand N^1-(4-(1H-1,2,4-triazole-1-yl)benzyl)-N^1-(2-aminoethyl)ethane-1,2-diamine (L) (Scheme 1) and employed it to react with Cd(II) salt to construct crystalline solid luminescent materials. As a result, a series of Cd-based MOFs decorated with chelating NH$_2$ sites were successfully achieved under solvothermal conditions: [Cd$_3$(BDC)$_3$(DMF)$_2$] (1), [Cd(L)(BDC)]$_2$·2DMF·H$_2$O (2), [Cd$_2$Na(L)(BDC)$_{2.5}$]·9H$_2$O (3), [Cd$_2$(L)(2,6-NDC)$_2$]·DMF·5H$_2$O (4) and [Cd$_2$(L)(BPDC)$_2$]·DMF·9H$_2$O (5). The results revealed that the dosage of NaOH can affect the coordination modes of L and dicarboxylate ligands to control the eventual structures of 1, 2 and 3. MOFs 3, 4 and 5 are three-dimensional (3D) frameworks and isolated by using different lengths of dicarboxylate auxiliary ligands (Scheme 1). The porosity and the fluorescence performance of 3, 4 and 5 make them potential fluorescent materials for detecting Fe(III) ions and antibiotics. The low detection limits for Fe(III) ions (155 ppb for 3, 209 ppb for 4 and 297 ppb for 5) and nitrofurazone (NZF) (162 ppb for 3, 75 ppb for 4 and 60 ppb for 5) illustrate that 3, 4 and 5 show a fast response and high sensitivity for trace amounts of Fe(III) and antibiotics. To our knowledge, this is the first example for probing antibiotics using Cd(II) luminescent MOFs.

2. Experimental

2.1 General information

All chemicals and solvents were of reagent grade, obtained from commercial sources without further purification. Antibiotics were purchased from Aladdin Industrial Corporation. Elemental analyses (EA) of C, H, and N were performed on a Perkin-Elmer 240C Elemental analyzer at the analysis center of Nanjing University. FT-IR spectra were recorded using KBr discs in the range of 400–4000 cm^{-1} on a Bruker Vector 22 FT-IR spectrophotometer. Thermogravimetric analyses (TGA) were carried out on a Mettler-Toledo (TGA/DSC1) thermal analyzer under nitrogen with a heating rate of 10 °C min^{-1}. Powder X-ray diffraction (PXRD) data were collected on a Bruker D8 Advance X-ray diffractometer with Cu Kα (λ = 1.5418 Å) radiation. The luminescence spectra of the powdered solid state samples were recorded on an Aminco Bowman Series 2 spectrofluorometer with a xenon arc lamp as the light source. In the measurements of emission and excitation spectra the pass width is 10 nm, and all the measurements were carried out under the same experimental

conditions. Quantum yields and luminescence lifetimes were obtained on a FluoroLog UltraFast spectrofluorometer analyzer with an integrating sphere. UV/vis absorption spectra were measured at room temperature on a UV3600 spectrophotometer.

2.2 Preparation of complexes 1–5

[Cd$_3$(BDC)$_3$(DMF)$_2$] (1). A mixture of L (9.37 mg, 0.036 mmol), H$_2$BDC (5.98 mg, 0.036 mmol), Cd(ClO$_4$)$_2$·6H$_2$O (25.16 mg, 0.06 mmol), and NaOH (0.58 mg, 0.014 mmol) in DMF/methanol/H$_2$O mixed solvent (4.5 mL, v/v/v: 3/1/0.5) was sealed in a 20 mL glass vial and heated at 90 °C for 72 h. After being cooled to room temperature, yellow block crystals of 1 were obtained in 40% yield. Elemental analysis calcd (%) for C$_{30}$H$_{26}$N$_2$O$_{14}$Cd$_3$: C 36.93, H 2.69, N 2.87; found: C 36.52, H 2.68, N 2.85.

[Cd(L)(BDC)]$_2$·2DMF·H$_2$O (2). Complex 2 was prepared by the same procedure used for the preparation of 1, except that the amount of NaOH was changed to 1.15 mg (0.029 mmol). Colorless crystals of 2 were obtained in 52% yield. Elemental analysis calcd (%) for C$_{48}$H$_{64}$N$_{14}$O$_{11}$Cd$_2$: C 46.57, H 5.21, N 15.84; found: C 46.52, H 5.28, N 15.85. IR (KBr pellet, cm^{-1}, Fig. S1 in the ESI†): 3405 (w), 3251 (w), 1662 (m), 1567 (s), 1523 (m), 1397 (s), 1280 (m), 1149 (w), 1052 (w), 982 (w), 945 (w), 890 (m), 854 (w), 826 (m), 746 (s), 673 (w), 661 (w), 508 (s).

[Cd$_2$Na(L)(BDC)$_{2.5}$]·9H$_2$O (3). Complex 3 was also achieved by the same procedure used for the synthesis of 1, except that NaOH (2.88 mg, 0.072 mmol) was used. Light yellow block crystals of 3 were obtained in 55% yield. Elemental analysis calcd (%) for C$_{33}$H$_{48}$N$_6$O$_{19}$NaCd$_2$: C 36.68, H 4.48, N 7.78; found: C 36.72, H 4.45, N 7.75. IR (KBr pellet, cm^{-1}, Fig. S1 in the ESI†): 3423 (w), 3269 (w), 1666 (m), 1566 (s), 1528 (w), 1504 (w), 1393 (s), 1313 (w), 1286 (w), 1223 (w), 1150 (w), 1094 (m), 1051 (w), 1015 (m), 978 (m), 945 (w), 889 (m), 843 (s), 826 (w), 747 (s), 675 (w), 662 (w), 520 (s).

[Cd$_2$(L)(2,6-NDC)$_2$]·DMF·5H$_2$O (4). 4 was isolated by the same procedure used for 3, except that 2,6-H$_2$NDC (7.78 mg, 0.036 mmol) was used instead of H$_2$BDC. After being cooled to room temperature, colorless crystals of 4 were obtained in 47% yield. Anal. calcd for C$_{40}$H$_{49}$N$_7$O$_{14}$Cd$_2$: C 44.62, H 4.59, N 9.11; found: C 44.65, H 4.58, N 9.15. IR (KBr pellet, cm^{-1}, Fig. S1 in the ESI†): 3406 (w), 3145 (w), 1668 (w), 1608 (m), 1567 (m), 1494 (w), 1402 (s), 1358 (w), 1277 (w), 1190 (w), 1139 (w), 1096 (w), 1049 (w), 976 (w), 929 (w), 887 (w), 852 (w), 791 (s), 673 (w), 447 (w).

[Cd$_2$(L)(BPDC)$_2$]·DMF·9H$_2$O (5). 5 was also obtained by the same procedure used for 3, except that H$_2$BPDC (8.72 mg, 0.036 mmol) was employed instead of H$_2$BDC. After being cooled to room temperature, colorless block crystals of 5 were obtained in 53% yield. Anal. calcd for C$_{44}$H$_{61}$N$_7$O$_{18}$Cd$_2$: C 44.01, H 5.12, N 8.17; found: C 44.05, H 5.18, N 8.15. IR (KBr pellet, cm^{-1}, Fig. S1 in the ESI†): 3263 (w), 3132 (w), 1664 (m), 1582 (s), 1527 (s), 1396 (s), 1280 (w), 1177 (w), 1145 (w), 1052 (w), 1006 (w), 978 (w), 854 (s), 774 (s), 679 (m).

2.3 Fluorescence study

In a typical experimental setup, 2 mg of 3, 4 or 5 was weighed and added to a cuvette containing 2.5 mL of DMF, and then

Table 1 Crystallographic data and structural refinements for **1**–**5**

Complex	1	2	3	4	5
Chemical formula	$C_{30}H_{26}N_2O_{14}Cd_3$	$C_{48}H_{64}N_{14}O_{11}Cd_2$	$C_{33}H_{30}N_6O_{10}NaCd_2$	$C_{37}H_{32}N_6O_8Cd_2$	$C_{41}H_{36}N_6O_8Cd_2$
Formula weight	975.73	1237.93	918.42	913.48	965.56
Temperature (K)	293(2)	293(2)	293(2)	293(2)	293(2)
Crystal system	Monoclinic	Triclinic	Triclinic	Triclinic	Monoclinic
Space group	$C2/c$	$P\bar{1}$	$P\bar{1}$	$P\bar{1}$	$C2/c$
$a/\text{Å}$	25.338(6)	10.7640(15)	9.8070(14)	10.9405(12)	24.068(3)
$b/\text{Å}$	9.524(2)	10.8279(15)	13.1382(19)	12.6609(13)	10.0444(13)
$c/\text{Å}$	18.120(4)	14.278(2)	18.607(3)	17.2175(18)	43.667(5)
$\alpha/°$	90	69.098(2)	89.278(2)	91.149(3)	90
$\beta/°$	129.684(3)	85.433(3)	76.577(2)	96.514(3)	92.677(2)
$\gamma/°$	90	64.744(2)	70.256(2)	112.944(3)	90
Volume/Å^3	3365.1(13)	1400.8(3)	2189.2(6)	2176.7(4)	10 545(2)
Z	4	1	2	2	8
$D_c/\text{g cm}^{-3}$	1.926	1.467	1.393	1.394	1.216
μ/mm^{-1}	1.949	0.827	1.034	1.028	0.852
$F(000)$	1904	634	914	912	3872
Reflections collected	14 325	9594	14 589	18 248	34 655
Unique reflections	3750	6369	9891	10 079	11 990
Parameters	252	345	470	478	524
Restraints	48	6	0	0	0
GOF	1.133	1.028	0.992	1.193	1.219
R_1, wR_2 $[I > 2\sigma(I)]^{a,b}$	$R_1 = 0.0288$, w$R_2 = 0.0835$	$R_1 = 0.0413$, w$R_2 = 0.1149$	$R_1 = 0.0445$, w$R_2 = 0.1144$	$R_1 = 0.0524$, w$R_2 = 0.1394$	$R_1 = 0.0736$, w$R_2 = 0.1630$
R_1, wR_2 (all data)	$R_1 = 0.0359$, w$R_2 = 0.0876$	$R_1 = 0.0510$, w$R_2 = 0.1217$	$R_1 = 0.0628$, w$R_2 = 0.1239$	$R_1 = 0.0756$, w$R_2 = 0.1486$	$R_1 = 0.0799$, w$R_2 = 0.1673$

^{a} $R_1 = \Sigma||F_o| - |F_c||/\Sigma|F_o|$. ^{b} w$R_2 = |\Sigma w(|F_o|^2 - |F_c|^2)|/\Sigma|w(F_o)^2|^{1/2}$, where w $= 1/[\sigma^2(F_o^2) + (aP)^2 + bP]$. $P = (F_o^2 + 2F_c^2)/3$.

dispersed ultrasonically. The solution was stirred at a constant rate to maintain homogeneity. All titrations were performed by gradual addition of selected analytes in an incremental fashion. Each titration was repeated three times to get a concordant value.

2.4 X-ray crystallography

Crystallographic data collections for **1**–**5** were carried out on a Bruker Smart Apex II CCD area-detector diffractometer with graphite-monochromated Mo Kα radiation ($\lambda = 0.71073$ Å) at 293(2) K using the ω-scan technique. The diffraction data were integrated by using the SAINT program,[33] which was also used for the intensity corrections for the Lorentz and polarization effects. Semi-empirical absorption corrections were applied using the SADABS program.[34] The structures were solved by direct methods and all the non-hydrogen atoms were refined anisotropically on F^2 using the full-matrix least-squares technique using the SHELXL-2014 crystallographic software package.[35,36] The hydrogen atoms except those of water molecules were generated geometrically and refined isotropically using the riding model. Atoms N1, O7, C13, C14 and C15 of the DMF molecule in **1** and N4, C32 and C33 atoms in **5** are disordered in two positions, each with a site occupancy of 0.50. Due to the highly disordered solvent molecules in **3**, **4** and **5**, their contribution to densities was modeled using the SQUEEZE routine in PLATON.[37,38] The final chemical formulae of **3**, **4** and **5** were obtained from crystallographic, EA and TG data. The details of the crystal parameters, data collection, and refinements for **1**–**5** are summarized in Table 1, selected bond lengths

and angles are listed in Table S1 in the ESI,† and hydrogen bonding data are given in Table S2 in the ESI.†

3. Results and discussion

Reactions of L, Cd(ClO$_4$)$_2$·6H$_2$O and H$_2$BDC/2,6-H$_2$NDC/H$_2$BPDC with different amounts of NaOH in a mixed solvent of DMF, methanol and water at 90 °C for 3 days yielded crystals **1**–**5**. The results show that the dosage of alkali (NaOH) in the reaction causes a great variation in the resulting structures since NaOH is alkali and can affect the deprotonation of the carboxylic acid ligands.[39]

3.1 Crystal structure of [Cd$_3$(BDC)$_3$(DMF)$_2$] (1)

Crystal structural analysis revealed that **1** crystallizes in the monoclinic space group $C2/c$ and the coordination environment around Cd(II) is shown in Fig. 1a. Notably, no ligand L was found in **1** probably because of the small amount of NaOH. Cd1 is coordinated by six carboxylate oxygen atoms (O1, O3, O4, O5, O6 and O6E) from four different BDC^{2-} ligands and one oxygen (O7) from a DMF molecule to give a distorted pentagonal bipyramidal coordination geometry, while Cd2 is surrounded by six carboxylate oxygen atoms (O2, O2A, O3, O3A, O4 and O4A). Moreover, two different BDC^{2-} ligands with $(\mu^2\text{-}\eta^1\text{:}\eta^2)$–$(\mu^2\text{-}\eta^1\text{:}\eta^2)$ and $(\mu^2\text{-}\eta^1\text{:}\eta^1)$–$(\mu^3\text{-}\eta^2\text{:}\eta^2)$ coordination modes (Fig. S2a and b in the ESI†) offer carboxylate oxygen atoms to coordinate with Cd1 and Cd2 atoms to form a Cd–O one-dimensional (1D) chain (Fig. 1b). The final structure of **1** is a 3D tubular-like framework with a diameter of 9.524 Å, which is
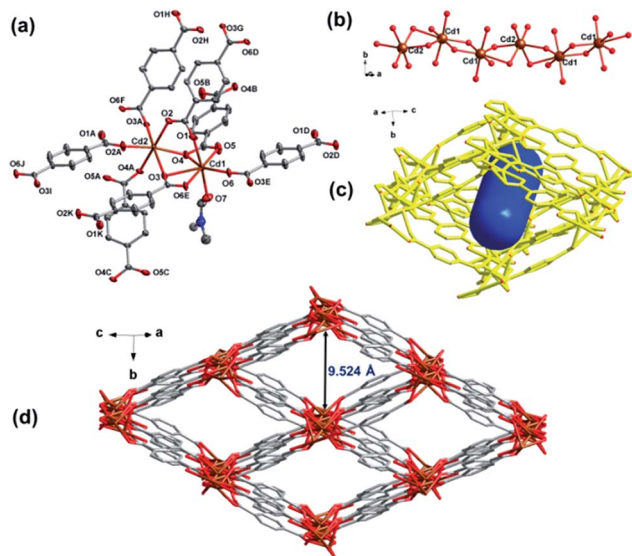
This journal is © The Royal Society of Chemistry 2017

J. Mater. Chem. A, 2017, **5**, 15797–15807 | **15799**

Fig. 1 (a) Coordination environment of Cd(ii) in **1** with ellipsoids drawn at the 30% probability level. Hydrogen atoms are omitted for clarity. (b) 1D Cd–O chain in **1**. (c) 3D tubular-like unit in **1**. (d) 3D framework of **1**. The coordinated DMF molecules are omitted for clarity.
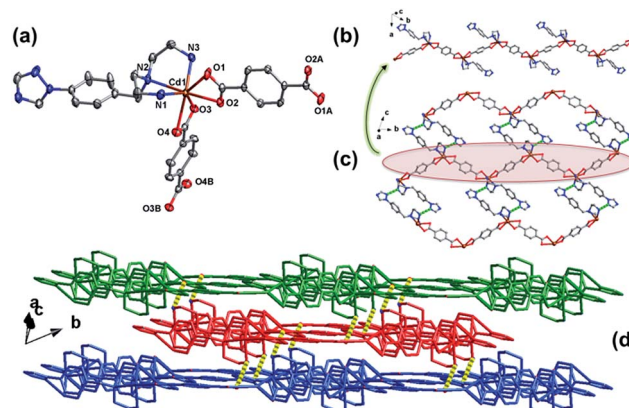

Fig. 2 (a) Coordination environment of Cd(ii) in **2** with ellipsoids drawn at the 30% probability level. Hydrogen atoms and non-coordinated solvent molecules are omitted for clarity. (b) 1D chain in **2**. (c) 2D layer of **2** with hydrogen bonds indicated by dashed lines. (d) 3D supramolecular structure of **2** with hydrogen bonds indicated by dashed lines (each color represents a 2D layer).

constructed by the Cd–O 1D chain and BDC^{2-} ligands (Fig. 1c and d). A similar framework has been reported previously in which aqua molecules, rather than the DMF, coordinated with Cd(ii).[40]

3.2 Crystal structure of $[Cd(L)(BDC)]_2 \cdot 2DMF \cdot H_2O$ (2)

When double amount of NaOH was used, complex **2** was isolated. In **2**, L acts as a terminal ligand offering the chelating nitrogen atoms to coordinate with Cd(ii). As illustrated in Fig. 2a, Cd1 adopts a coordination donor set of N_3O_4, which comprises three chelating nitrogen atoms (N1, N2 and N3) from one L, and four carboxylate oxygen ones (O1, O2, O3 and O4) from two different BDC^{2-} ligands. Meanwhile, the carboxylate groups of BDC^{2-} with $(\mu^1\text{-}\eta^1\text{:}\eta^1)\text{-}(\mu^1\text{-}\eta^1\text{:}\eta^1)$ coordination mode (Fig. S2c in the ESI†) connect Cd atoms to produce a 1D chain (Fig. 2b), which is connected through N–H···N hydrogen bonds (N1···N5 = 3.360 Å) (Fig. S3a in the ESI†) to extend into a two-dimensional (2D) network (Fig. 2c). The 2D layers further connect each other by N–H···O hydrogen bonds (N3···O2 = 3.062 Å) (Fig. S3b in the ESI†) to give a 3D supramolecular structure of **2** (Fig. 2d).

3.3 Crystal structure of $[Cd_2Na(L)(BDC)_{2.5}] \cdot 9H_2O$ (3)

When the dosage of NaOH is further raised up to 0.072 mmol, **3** with an entirely different structure was successfully obtained. The asymmetric unit of **3** contains two Cd(ii), one Na(i) ion, one L, two and a half BDC^{2-} and nine free water molecules. Fig. 3a shows that Cd1 is seven coordinated by three chelating nitrogen atoms (N1, N2 and N3) and four oxygen ones (O1, O2, O3 and O4), whereas Cd2 is also seven coordinated by three pairs of chelating carboxylate groups (O5D, O6D, O7, O8, O9 and O10) from three BDC^{2-} moieties and one triazole nitrogen

(N6) from the L ligand. The Cd–N distances are from 2.280(5) to 2.597(4) Å, while the Cd–O ones are in a range of 2.269(3)– 2.560(3) Å, which are well-matched to those observed in the reported Cd(ii) complexes.[41] It is noteworthy that the Na ions in **3** connect Cd(ii) atoms through carboxylate oxygen atoms to give a $[Na_2Cd_4]$ sub-unit (Fig. 3b and c), which is further linked by BDC^{2-} to generate an infinite 1D chain (Fig. S4 in the ESI†). Adjacent 1D chains are further extended to form a 2D network by carboxylate oxygen through the BDC^{2-} ligand with $(\mu^2\text{-}\eta^1\text{:}\eta^2)\text{-}(\mu^2\text{-}\eta^1\text{:}\eta^2)$ mode (Fig. S2d in the ESI† and 3d). Subsequently, L acts as the bridging ligand to further link the 2D layers through Cd–N bonds to generate the final 3D structure of **3** with irregular channels (Fig. S5 in the ESI† and 3e). Considering the existence of nine free water molecules per unit, the PLATON program was used to calculate the solvent-accessible volume. It was approximately 726.5 Å^3 per 2189.2 Å^3 unit cell volume, and the pore volume ratio is calculated to be 33.2%.

3.4 Crystal structure of $[Cd_2(L)(2,6\text{-}NDC)_2] \cdot DMF \cdot 5H_2O$ (4)

When the dicarboxylate ligand H$_2$BDC was replaced by longer ones 2,6-H$_2$NDC and H$_2$BPDC, **4** and **5** were isolated. As shown in Fig. 4a, Cd1 in **4** is bound by seven oxygen atoms from three pairs of chelating carboxylate groups (O1, O2, O5, O6, O7 and O8) and one bridging oxygen (O3), while Cd2 is five-coordinated with a coordination donor set of N_4O, which comprises three chelating nitrogen atoms (N1, N2 and N3), one triazole nitrogen (N4) from two L ligands and one bridging oxygen atom (O4) from one 2,6-NDC^{2-}. The bond distances around Cd(ii) are 2.252(6)–2.460(4) Å for Cd–N and 2.249(3)–2.631(5) Å for Cd–O. In **4**, the 2,6-NDC^{2-} ligand acts as a μ^2-bridging linker with $(\mu^1\text{-}\eta^1\text{:}\eta^1)\text{-}(\mu^1\text{-}\eta^1\text{:}\eta^1)$ coordination mode (Fig. S6a in the ESI†) to connect two Cd(ii) atoms to form a 2D Cd-NDC network, which contains a hexagon of diameter 16.815 Å (Fig. 4b). Meanwhile, Cd2 atoms and L ligands are constructed into a 1D Cd–L chain

15800 | *J. Mater. Chem. A*, 2017, **5**, 15797–15807

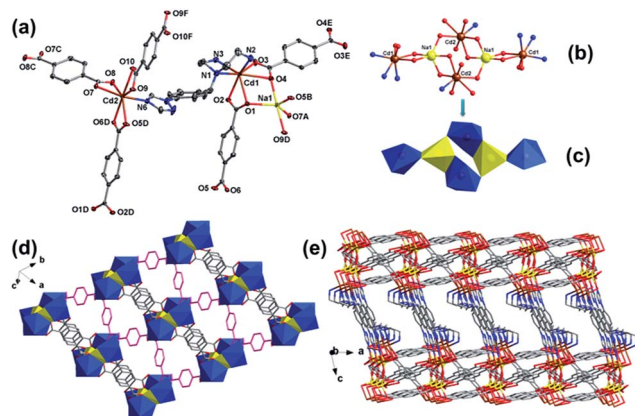This journal is © The Royal Society of Chemistry 2017

Fig. 3 (a) Coordination environment of Cd(II) in **3** with ellipsoids drawn at the 30% probability level. Hydrogen atoms and free water molecules are omitted for clarity. (b) [Na_2Cd_4] unit in **3**. (c) Polyhedral view of the [Na_2Cd_4] unit. (d) 2D layer with [Na_2Cd_4] units in **3**. (e) 3D structure of **3**.

(Fig. 4c). The combination of the 1D Cd–L chain and 2D Cd–NDC network generated the final 3D structure of **4** filled with another 2,6-NDC^{2-} ligand with (μ^1-η^1:η^1)–(μ^2-η^1:η^1) mode (Fig. S6b in the ESI† and 4d). There are channels with a diameter of 9.147 Å. PLATON calculations suggest that the resulting effective free volume, after the removal of non-coordinated water and DMF molecules, is 30.1% (655.0 Å^3 per 2176.7 Å^3 unit crystal volume).

3.5 Crystal structure of [$Cd_2(L)(BPDC)_2$]·DMF·$9H_2O$ (5)

Complex **5** crystallizes in the monoclinic space group $C2/c$, rather than triclinic $P\bar{1}$ in **4**; however, the coordination environment around Cd(II) in **5** is similar to that in **4** (Fig. 5a). In **5**,

a 2D hexagonal network which was built by metal ions and dicarboxylate ligands was also observed. The difference between the 2D hexagonal networks in **4** and **5** is the distance between the hexagon sides: the largest distance between the two sides of the hexagon in **5** is 24.068 Å which is larger than the one in **4** (16.815 Å) due to the longer dicarboxylate ligand (H_2BPDC) (Fig. 5b). Furthermore, there are cages with a diameter of 11.774 Å in the 3D framework of **5** (Fig. 5c and d) and the high-solvent accessible volume in **5** is 3977.1 Å^3 out of the 10 545.0 Å^3 unit cell volume (37.7% of the total crystal volume) calculated by PLATON.

3.6 Powder X-ray diffraction (PXRD) and thermal stability

The phase purity of the as-synthesized samples was further confirmed by PXRD measurements, and each PXRD pattern of the as-synthesized samples is consistent with the simulated ones (Fig. S7 in the ESI†), implying the pure phases of **2–5**. Complexes **2–5** are air stable, and their thermal stability was investigated in the temperature range of 30–800 °C by TG measurements under a nitrogen atmosphere (Fig. S8 in the ESI†). **2** shows a weight loss of 13.04% in the range of 30–220 °C, which corresponds to the loss of free water and DMF molecules (calcd 13.26%), and a further weight loss was observed at about 300 °C, corresponding to the collapse of the framework. **3** loses 14.99% of weight in the temperature range of 30–180 °C, which is attributed to the departure of the free water molecules (calcd 15.00%), and the residue can be stable up to about 320 °C. A weight loss of 15.22% was observed for **4** in the temperature range of 30–280 °C due to the loss of the free water and DMF molecules (calcd 15.15%), and the decomposition of the framework occurred at about 300 °C. The TG curve of **5** shows a weight loss of 19.49% in the temperature range of 30–280 °C,
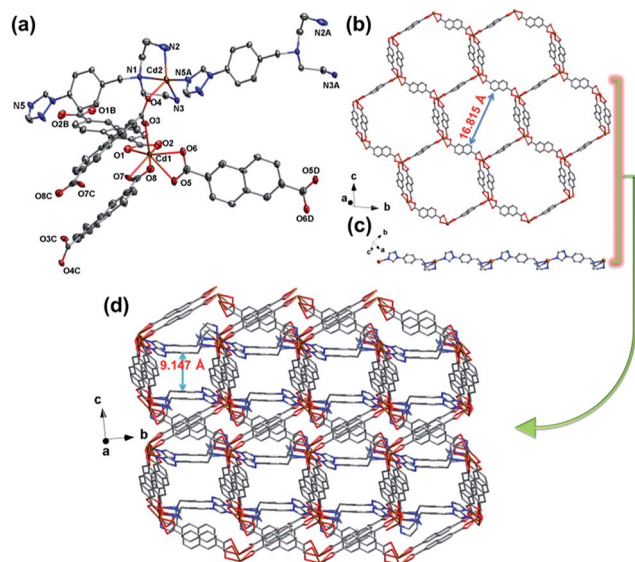

Fig. 4 (a) Coordination environment of Cd(II) in **4** with ellipsoids drawn at the 30% probability level. Hydrogen atoms and non-coordinated solvent molecules are omitted for clarity. (b) 2D Cd–NDC network in **4**. (c) 1D Cd–L chain in **4**. (d) 3D structure of **4**.
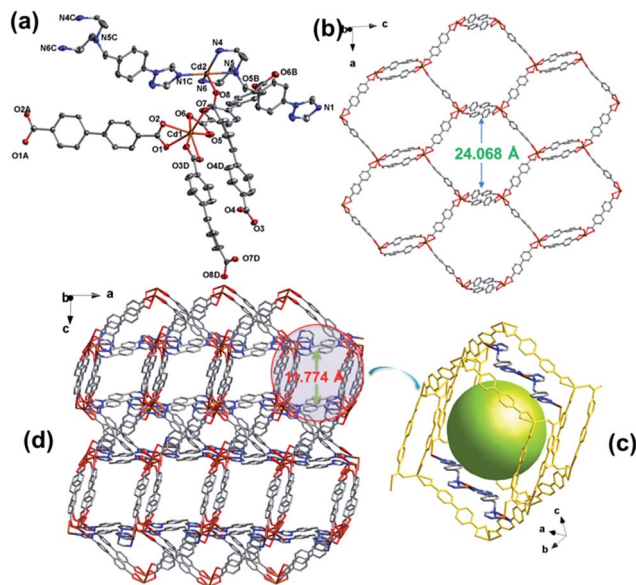

Fig. 5 (a) Coordination environment of Cd(II) in **5** with ellipsoids drawn at the 30% probability level. Hydrogen atoms and non-coordinated solvent molecules are omitted for clarity. (b) 2D network in **5**. (c) Cage unit in **5**. (d) 3D structure of **5** with cages of diameter 11.774 Å.

corresponding to the release of free water together with DMF molecules (calcd 19.59%), and then the framework was gradually decomposed above 300 °C.

3.7 Photoluminescence properties

MOFs constructed from d^{10}-metal ions and conjugated organic ligands are promising candidates for potential luminescent materials.[42–46] The solid state photoluminescence (PL) properties of ligand L and **2**, **3**, **4**, and **5** were studied at room temperature (Fig. S9 in the ESI†). Intense emission bands were observed at $\lambda_{em} = 430$ nm ($\lambda_{ex} = 326$ nm) for **2**, 420 nm ($\lambda_{ex} = 326$ nm) for **3**, 395 nm ($\lambda_{ex} = 345$ nm) for **4** and 389 nm ($\lambda_{ex} = 326$ nm) for **5**. The ligand L exhibits fluorescence emission at 480 nm upon excitations at 400 nm. Compared with the free ligand L, fluorescence intensities of **2–5** show apparent fluorescence enhancement implying that the formation of MOFs enhances the fluorescence of the ligand. This is known as aggregation-induced emission (AIE), which is considered to be caused by the coordination of organic ligands to metal ions that restricts the deformation of the ligand and induces nonradiative relaxation.[47] Meanwhile, compared with the free L ligand, **2–5** show obvious blue-shifted emissions which can be tentatively ascribed to metal–ligand coordination interactions. Absolute quantum yields of **3**, **4** and **5** are 2.06%, 5.90% and 5.33%, respectively. The high absolute quantum yields of **4** and **5** may be attributed to the conformational rigidity of the frameworks to reduce the non-radiative relaxation process.[48]

3.8 Chemosensor for Fe(III) ions

Considering that the NH_2 group in luminescent MOF materials is an electron-donating group and can bind metal ions, the application of **3–5** as luminescent probes for sensing metal ions was explored. First, stable suspension solutions used for fluorescence measurements were obtained by immersing fresh samples in different organic solvents. It is well known that in such ligand-based emission systems, organic ligands absorb energy upon excitation to give the corresponding fluorescence; however, in the presence of small solvent molecules, energy transfer between the organic ligands and solvent molecules may occur and cause the quenching of the fluorescence.[49] As shown in Fig. S10 in the ESI,† the fluorescence emissions of **3** have a slight dependence on the solvent molecules excited at 326 nm; however, the fluorescence emissions of **4** and **5** are largely dependent on the solvent molecules excited at 345 and 326 nm, respectively. This phenomenon is to a great extent ascribed to the stability of the framework and the interactions between the framework and solvent molecules.[50,51] For **4**, the photoluminescence intensity depends on the identity of the solvent molecule with the sequence of DMF > NMP > 2-PA > CH_3CN > THF > CH_2Cl_2 > $CHCl_3$ > acetone > EtOH > MeOH, while for **5**, the sequence is DMF > 2-PA > NMP > EtOH > MeOH > CH_2Cl_2 > $CHCl_3$ > CH_3CN > THF > acetone. Both **4** and **5** represent excellent fluorescence emissions in the suspensions of DMF, being promising candidates for detection applications in the solution phase.

The good fluorescence performances of **3**, **4** and **5** in suspension prompt us to explore their fluorescence sensing properties by using DMF as the dispersion medium. A series of spectroscopic measurements have been conducted to explore the fluorescence responses of MOFs **3**, **4** and **5** with different metal ions in DMF suspension. For comparison, the finely ground samples of **3**, **4** and **5** (2 mg) were dispersed in 2.5 mL DMF solutions containing $M(NO_3)_x$ (1 mM, M = K^+, Na^+, Ni^{2+}, Ca^{2+}, Li^+, Sr^{2+}, Sm^{3+}, Mn^{2+}, Zn^{2+}, Co^{2+}, Pb^{2+}, Cu^{2+}, Cr^{3+}, Al^{3+}, Fe^{3+}) to form metal ion incorporated MOF suspensions for luminescence studies. As shown in Fig. 6, the luminescence intensities of **3**, **4** and **5** have been quenched to some extent for all metal ions, but the quenching level is dependent on the species of metal ions. Among the metal ions studied, the quenching effects of Al^{3+} and Fe^{3+} are very pronounced, especially for Fe(III) ions.

In order to assess the sensing sensitivity of **3**, **4** and **5**, quantitative fluorescence titration experiments were performed. Interestingly, the luminescence intensity of Fe(III)-incorporated **3**, **4** and **5** is heavily dependent on the concentration of the metal ions. As shown in Fig. 7a–c, the emission intensity decreased monotonically and drastically when the Fe(III) concentration increased from 0 μL to 680 μL. It is remarkable that MOFs **3**, **4** and **5** feature highly sensitive and selective sensing for Fe(III) ions in DMF suspension. The quenching effects of **3**, **4** and **5** were examined as a function of $Fe(NO_3)_3$ concentration in the range of 0–0.1 mM. The fluorescence quenching efficiency can be quantitatively explained by the Stern–Volmer (SV) equation: $(I_0/I) = 1 + K_{sv}[M]$, where K_{sv} is the quenching constant (M^{-1}), [M] is the molar concentration of the analyte, and I_0 and I are the luminescence intensities before and after addition of the analyte, respectively. A detailed SV analysis further revealed that there exists a good linear correlation ($R_2 = 0.9989$ for **3**, $R_2 = 0.9998$ for **4**, and $R_2 = 0.9985$ for **5**) between the quenching efficiency and the amount of Fe(III) in the low concentration range (from 0 to 0.03 mM), as indicated in Fig. 7a–c (inset). Moreover, when the concentration of Fe(III) increased to 0.21 mM, the quenching efficiency could almost reach 100%. On the basis of the experimental data in Fig. 7, the K_{sv} values are calculated to be 1.67×10^4 M^{-1} for **3**, 1.44×10^4 M^{-1} for **4**, and 1.08×10^4 M^{-1} for **5**. Based on the K_{sv} values and
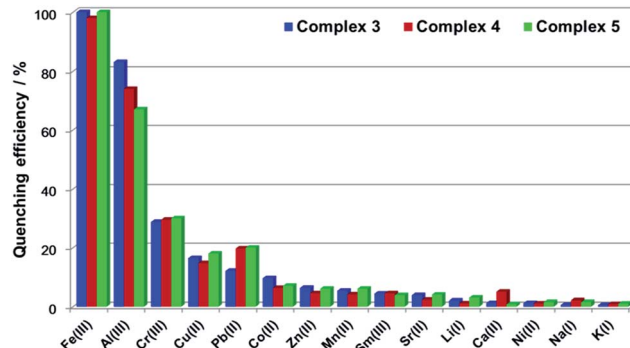

Fig. 6 Luminescence quenching efficiency of **3**, **4** and **5** in the presence of different metal ions.

15802 | *J. Mater. Chem. A*, 2017, **5**, 15797–15807
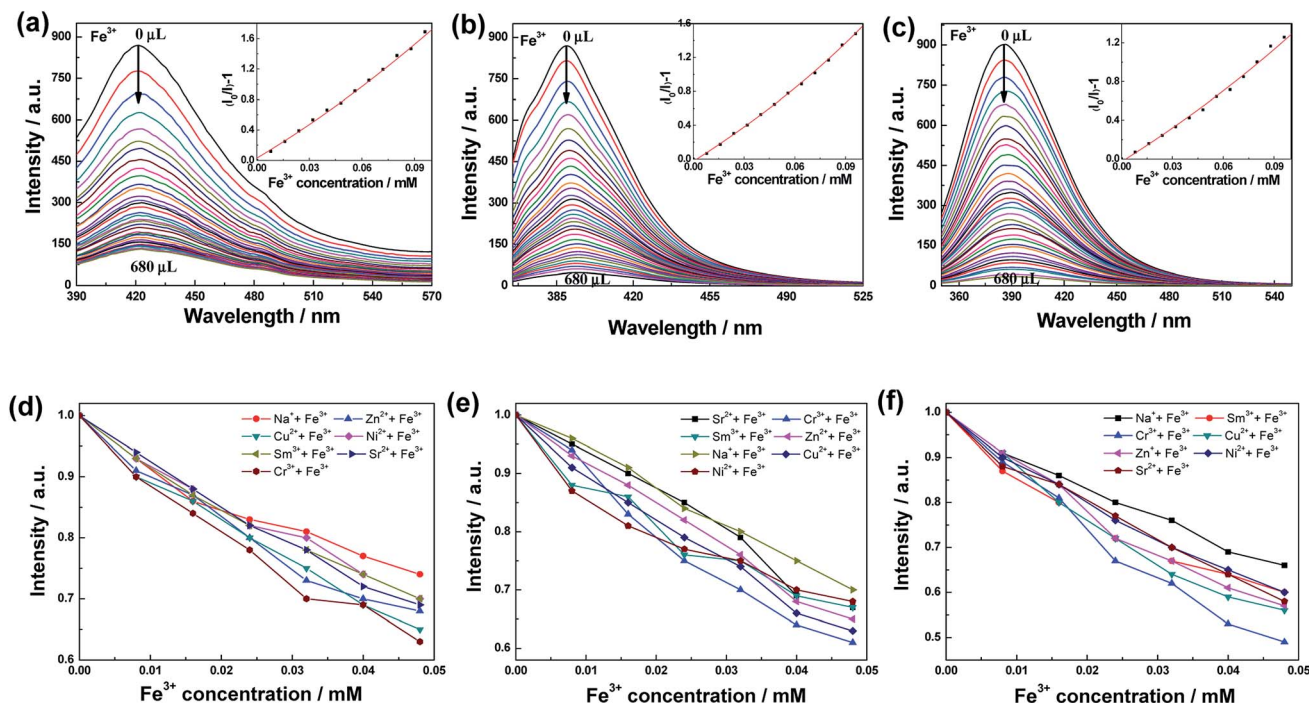
This journal is © The Royal Society of Chemistry 2017

Fig. 7 Effect on the emission spectra of 3 (a), 4 (b) and 5 (c) dispersed in DMF suspensions upon incremental addition of Fe(III) ions (1 mM, 20 μL addition each time; inset: SV plots of Fe(III) ions) and selective detection of Fe(III) ions on 3 (d), 4 (e) and 5 (f) in the presence of other metal ions in DMF suspensions.

the standard error (σ) for three repeated fluorescence measurements of blank solutions, the detection limits ($3\sigma/K_{sv}$) are calculated to be 155 ppb for 3, 209 ppb for 4, and 297 ppb for 5, which are a clear indication of the high sensing sensitivity of 3, 4 and 5 towards Fe(III). As shown in Table S3 in the ESI,† compared with reported Cd–MOFs, the K_{sv} values of 3, 4 and 5 are relatively good under the same conditions.[8,9,52]

For comparison, fluorescence titration experiments of Al(III)-incorporated 3, 4 and 5 were also performed. As shown in Fig. S11 in the ESI,† the calculated K_{sv} values are 4.48×10^3 M^{-1} for 3, 4.36×10^3 M^{-1} for 4, and 2.52×10^3 M^{-1} for 5. Accordingly, the $K_{sv}[\text{Fe(III)}]/K_{sv}[\text{Al(III)}]$ values are 3.73, 3.30 and 4.29 for metal ion-incorporated 3, 4 and 5, respectively. The results imply that 3, 4 and 5 show highly selective sensing for Fe(III) ions.

Usually, many metal ions coexist in a practical biological and environmental system. Considering the high sensing sensitivity of 3, 4, 5 towards Fe(III), we further checked the detection selectivity for Fe(III) in the presence of other metal ions by fluorescence spectra. In the control experiment, a 1 mM DMF solution of M(NO$_3$)$_x$ (M = Cr^{3+}, Sm^{3+}, Cu^{2+}, Zn^{2+}, Sr^{2+}, Ni^{2+} and Na$^+$) was initially added to the DMF suspensions of 3, 4 and 5, followed by addition of Fe(III) (20 μL). With increasing Fe(III) concentration (from 0 to 0.048 mM), the fluorescence emissions of 3, 4 and 5 are quenched efficiently. These results can be easily visualized by plotting the percentage fluorescence intensity *versus* the concentration of Fe(III) added, as shown in Fig. 7d–f, where the stepwise decrease in fluorescence intensity clearly demonstrates the selectivity of 3, 4 and 5 toward Fe(III).

3.9 Chemosensor for antibiotics

Antibiotics, being used extensively for the treatment of bacterial infections in humans and animals, have been considered as a class of important organic pollutants. Therefore, rapid probing of antibiotics is of great significance from the viewpoint of human health and environmental protection. Considering the excellent luminescence behaviors and high porosities of 3, 4 and 5, it will be of great interest to apply them as potential fluorescent sensors for detecting antibiotics such as NFs (nitrofurazone, NZF; nitrofurantoin, NFT; furazolidone, FZD), NMs (metronidazole, MDZ; dimetridazole, DTZ), sulfonamides (sulfadiazine, SDZ; sulfamethazine, SMZ), chloramphenicols (thiamphenicol, THI) and β-lactams (penicillin, PCL) (Fig. S12 in the ESI†). To explore the ability of 3, 4 and 5 to sense a trace quantity of antibiotics, fluorescence-quenching titrations were performed by gradual addition of antibiotics to DMF suspensions of 3, 4 and 5. During the titration experiments, the as-synthesized samples of 3, 4 or 5 (2 mg) in DMF solvent (2.5 mL), and then upon incremental addition of a selected antibiotic (1 mM, 20 μL addition each time). The percentage of fluorescence quenching in terms of a certain amount of different antibiotics at room temperature is depicted in Fig. 8. Obviously, the sensing experiments show that high fluorescence quenching of MOFs occurs upon the incremental addition of NZF, and the order of quenching efficiency is NZF > NFT > FZD > MDZ > DTZ > SDZ > THI > PCL > SMZ for 3, NZF > NFT > FZD > MDZ > DTZ > THI > SDZ > SMZ > PCL for 4, and NZF > NFT > FZD > DTZ > SMZ > SDZ > THI > PCL for 5. NZF, NFT and FZD give rise to the highest quenching efficiencies of 93, 83 and 69% for 3, 99,
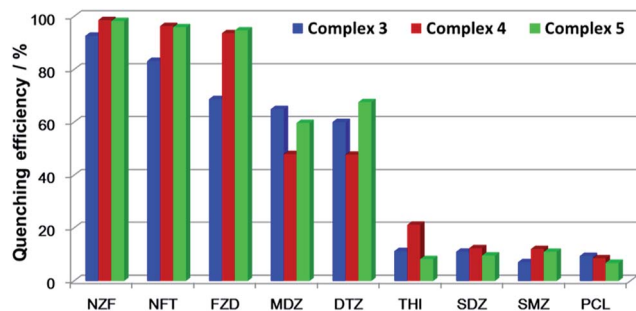
Fig. 8 Fluorescence quenching of **3**, **4** and **5** by different antibiotics at room temperature.

96 and 94% for **4**, and 98, 96 and 95% for **5**, respectively. In addition, MDZ and DTZ also lead to relatively high quenching efficiencies, whereas quenching efficiencies are low for the remaining antibiotics (Fig. 9a–c and S13–S18 in the ESI†).

It is demonstrated that **3**, **4** and **5** have high quenching efficiencies toward NFs, but very poor quenching efficiencies toward PCL antibiotics. Motivated by these findings, we further checked the detection selectivity for NFs in the presence of PCL. To these systems, a saturated DMF solution of PCL was initially added to the DMF suspensions of **3**, **4** and **5**, so that high-affinity binding sites would be accessible to PCL followed by addition of NFs (20 μL). As can be seen from Fig. S19–S21 in the ESI,† the emission intensity of the three MOFs only shows slight changes in the presence of excess PCL. Upon introducing NFs into the mixture of the MOFs and PCL, the fluorescence was

significantly quenched. This result reveals that the interference from PCL can be neglected, supporting the high quenching selectivity of the three MOFs toward NFs. The results can be easily visualized by plotting the percentage fluorescence intensity *versus* the volume of antibiotics added, where the stepwise decrease in fluorescence intensity clearly demonstrates the selectivity of **3**, **4** and **5** toward NFs, even in the presence of a higher concentration of PCL (Fig. S22 in the ESI†).

Similar to the titration experiments in identity of the metal ions, the fluorescence intensity *vs.* antibiotics plot close to the Stern–Volmer equation (Fig. 9d–f). The SV plots for NFs are nearly linear in low concentration ranges (from 0 to 0.03 mM), however deviate from linearity and bend upward when the concentration increases. Such phenomena of nonlinear SV plots may be attributed to self-absorption or an energy-transfer process. All the other antibiotics showed linear SV plots during the tested concentration ranges. On the basis of the experimental data in Fig. 9 (inset) and Fig. S13, S15 and S17 (inset) in the ESI,† the K_{sv} values of **3** are calculated to be 5.06×10^4 M^{-1} for NZF, 3.57×10^4 M^{-1} for NFT, and 1.83×10^4 M^{-1} for FZD. The K_{sv} values of **4** are calculated to be 1.04×10^5 M^{-1} for NZF, 7.19×10^4 M^{-1} for NFT, and 6.38×10^4 M^{-1} for FZD. The K_{sv} values of **5** are calculated to be 1.33×10^5 M^{-1} for NZF, 6.93×10^4 M^{-1} for NFT, and 5.40×10^4 M^{-1} for FZD. The detection limits of **3**, **4**, and **5** toward NZF were 162, 75 and 60 ppb, respectively (Tables S4 in the ESI† and 2), which are comparable to the values of 50–90 ppb for the reported Zr(ɪᴠ)–MOFs.[53] To our knowledge, this work is the first example for probing antibiotics using Cd(ɪɪ) luminescent materials since the first reported Zr(ɪᴠ)–MOF antibiotics probe.[53]
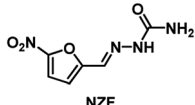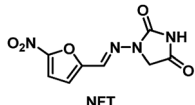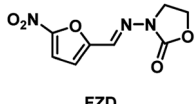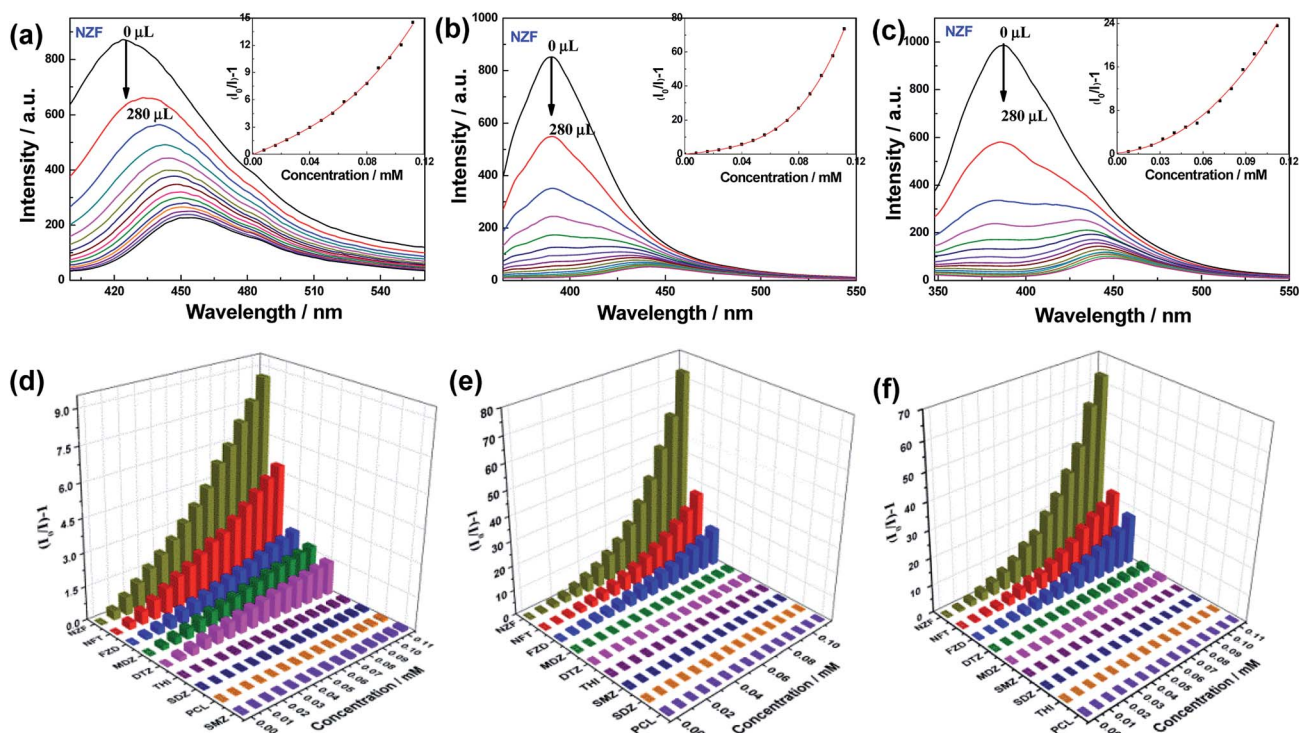

Fig. 9 Effect on the emission spectra of **3** (a), **4** (b) and **5** (c) dispersed in DMF solutions upon incremental addition of selected antibiotics (1 mM, 20 μL addition each time; inset: SV plots of selected antibiotics) and Stern–Volmer plots of selected antibiotics in **3** (d), **4** (e) and **5** (f).

15804 | *J. Mater. Chem. A*, 2017, **5**, 15797–15807

This journal is © The Royal Society of Chemistry 2017

Table 2 K_{sv}, standard error, and detection limits of **3**, **4** and **5** toward NZF, NFT and FZD at room temperature

Antibiotics	K_{sv} (M^{-1})			Standard error (σ)			Detection limit (ppb)		
	3	4	5	3	4	5	3	4	5
NZF	5.06×10^4, ($R^2 = 0.99932$)	1.04×10^5, ($R^2 = 0.97162$)	1.33×10^5, ($R^2 = 0.97851$)	0.0131	0.0124	0.0127	162	75	60
NFT	3.57×10^4, ($R^2 = 0.99948$)	7.19×10^4, ($R^2 = 0.99173$)	6.93×10^4, ($R^2 = 0.99458$)	0.0130	0.0125	0.0131	274	131	142
FZD	1.83×10^4, ($R^2 = 0.99954$)	6.38×10^4, ($R^2 = 0.99988$)	5.40×10^4, ($R^2 = 0.98077$)	0.0127	0.0128	0.0129	494	143	170

3.10 Mechanism for probing Fe(III) ions and antibiotics

To understand the mechanism of the fluorescence quenching effect of **3**, **4** and **5** toward Fe(III) ions and antibiotics, further experiments were carried out. The luminescence lifetimes of **3**, **4** and **5** before and after the addition of Fe(III) are almost the same, and the results show that there is no coordination between the metal ions and MOFs (Fig. S23–S25 in the ESI†). In addition, the UV/vis absorption data of **3**, **4**, and **5** and varied metal ions show that the wide absorption band from 230 to 500 nm of Fe(III) covers the range of absorption bands of **3**, **4** and **5**, and is much more strongly than those of other metal ions (Fig. S26 in the ESI†). This means that the UV/vis absorption of Fe(III) upon excitation may prevent the absorption of **3**, **4** and **5**, and result in the decrease or quenching of the luminescence.[54–56] As for the antibiotics, upon excitation, the excited electron from the conduction-band (CB) of the MOF may transfer to the lowest unoccupied molecular orbital (LUMO) of the antibiotics, thus resulting in fluorescence quenching.[57,58] The efficient fluorescence quenching observed for NFs (NZF, NFT and FZD) is consistent with the low LUMO energy of NFs calculated by DFT (Table S5 and Fig. S27 in the ESI†). In addition, the nonlinearity trend of the SV plots for NFs mentioned above indicates that there may be an energy transfer mechanism in the fluorescence quenching processes,[59] since the UV/vis absorption band of NFs has the greatest degree of overlapping with the emission spectra of **3**, **4** and **5** (Fig. S28 in the ESI†). As a result, the coexistence of electron transfer and energy transfer enables NFs to have a high photoluminescence quenching effect compared with other studied antibiotics.

4. Conclusions

In summary, we designed and synthesized a series of luminescent Cd-based metal–organic probes decorated with chelating NH$_2$ sites based on a new amino triazole ligand and d^{10} Cd(II) ions. Frameworks **1**, **2** and **3** revealed that the dosage of NaOH can affect the coordination mode of both the ligand L and

carboxylate auxiliary ligand to control the final structures. Moreover, by increasing the length of the carboxylate ligand, frameworks **4** and **5** with lager channels were fabricated. The porosities and the good fluorescence performances of **3**, **4** and **5** make them potential fluorescent materials which can be used to detect Fe(III) ions and antibiotics. The low detection limits for Fe(III) ions (155 ppb for **3**, 209 ppb for **4** and 297 ppb for **5**) and NZF (162 ppb for **3**, 75 ppb for **4** and 60 ppb for **5**) illustrate that **3**, **4** and **5** show a fast response and high sensitivity for trace amounts of Fe(III) and antibiotics. The absorption of Fe(III) between 230 and 500 nm hindered the absorption of **3**, **4** and **5** and caused photoluminescence attenuation of **3**, **4** and **5**. The high quenching efficiencies for the antibiotics may be attributed to the coexistence of electron transfer and resonance energy transfer in antibiotic detection processes. To our knowledge, this is the first example for probing antibiotics using Cd(II) luminescent MOFs.

Notes and references

1. S. K. Sahoo, D. Sharma, R. K. Bera, G. Crisponi and J. F. Callan, *Chem. Soc. Rev.*, 2012, **41**, 7195–7227.
2. Q. Zhao, F. Y. Li and C. H. Huang, *Chem. Soc. Rev.*, 2010, **39**, 3007–3030.
3. X. Y. Xu and B. Yan, *ACS Appl. Mater. Interfaces*, 2015, 7, 721–729.

This journal is © The Royal Society of Chemistry 2017

J. Mater. Chem. A, 2017, **5**, 15797–15807 | **15805**

4   Z. Chen, Y. Sun, L. Zhang, D. Sun, F. Liu, Q. Meng, R. Wang and D. Sun, *Chem. Commun.*, 2013, **49**, 11557–11559.

5   Y. Zhou, H. H. Chen and B. Yan, *J. Mater. Chem. A*, 2014, **2**, 13691–13697.

6   X. Y. Dong, R. Wang, J. Z. Wang, S. Q. Zang and T. C. W. Mak, *J. Mater. Chem. A*, 2015, **3**, 641–647.

7   Q. Tang, S. Liu, Y. Liu, J. Miao, S. Li, L. Zhang, Z. Shi and Z. Zheng, *Inorg. Chem.*, 2013, **52**, 2799–2801.

8   Y. L. Wu, G. P. Yang, Y. D. Zhang, N. N. Shi, J. Han and Y. Y. Wang, *RSC Adv.*, 2015, **5**, 90772–90777.

9   Y. L. Wu, G. P. Yang, X. Zhou, J. Li, Y. Ning and Y. Y. Wang, *Dalton Trans.*, 2015, **44**, 10385–10391.

10 X. Liu, J. C. Steele and X. Z. Meng, *Environ. Pollut.*, 2017, **223**, 161–169.

11 K. Kümmerer, *Chemosphere*, 2009, **75**, 417–434.

12 Q. Q. Zhang, G. G. Ying, C. G. Pan, Y. S. Liu and J. L. Zhao, *Environ. Sci. Technol.*, 2015, **49**, 6772–6782.

13 A. P. de Silva, H. Q. N. Gunaratne, T. Gunlaugsson, A. J. M. Huxley, C. P. McCoy, J. T. Rademacher and T. E. Rice, *Chem. Rev.*, 1997, **97**, 1515–1566.

14 Y. J. Cui, Y. F. Yue, G. D. Qian and B. L. Chen, *Chem. Rev.*, 2012, **112**, 1126–1162.

15 L. E. Kreno, K. Leong, O. K. Farha, M. Allendorf, R. P. Van Duyne and J. T. Hupp, *Chem. Rev.*, 2012, **112**, 1105–1125.

16 Y. L. Li, Y. Zhao, P. Wang, Y. S. Kang, Q. Liu, X. D. Zhang and W. Y. Sun, *Inorg. Chem.*, 2016, **55**, 11821–11830.

17 J. W. Ye, L. M. Zhao, R. F. Bogale, Y. Gao, X. X. Wang, X. M. Qian, S. Guo, J. Z. Zhao and G. L. Ning, *Chem.–Eur. J.*, 2015, **21**, 2029–2037.

18 Y. L. Hou, H. Xu, R. R. Cheng and B. Zhao, *Chem. Commun.*, 2015, **51**, 6769–6772.

19 Z. C. Hu, B. J. Deibert and J. Li, *Chem. Soc. Rev.*, 2014, **43**, 5815–5840.

20 Y. Q. Dong, J. H. Cai, Q. Q. Fang, X. You and Y. W. Chi, *Anal. Chem.*, 2016, **88**, 1748–1752.

21 J. H. Lee, J. Jaworski and J. H. Jung, *Nanoscale*, 2013, **5**, 8533–8540.

22 S. S. Zhao, J. Yang, Y. Y. Liu and J. F. Ma, *Inorg. Chem.*, 2016, **55**, 2261–2273.

23 Y. Guo, X. Feng, T. Han, S. Wang, Z. Lin, Y. Dong and B. Wang, *J. Am. Chem. Soc.*, 2014, **136**, 15485–15488.

24 J. W. Ye, H. L. Zhou, S. Y. Liu, X. N. Cheng, R. B. Lin, X. L. Qi, J. P. Zhang and X. M. Chen, *Chem. Mater.*, 2015, **27**, 8255–8260.

25 M. Formica, V. Fusi, L. Giorgi and M. Micheloni, *Coord. Chem. Rev.*, 2012, **256**, 170–192.

26 S. K. Sahoo, D. Sharma, R. K. Bera, G. Crisponi and J. F. Callan, *Chem. Soc. Rev.*, 2012, **41**, 7195–7227.

27 M. Zheng, H. Q. Tan, Z. G. Xie, L. G. Zhang, X. B. Jing and Z. C. Sun, *ACS Appl. Mater. Interfaces*, 2013, **5**, 1078–1083.

28 B. L. Chen, L. B. Wang, Y. Q. Xiao, F. R. Fronczek, M. Xue, Y. J. Cui and G. D. Qian, *Angew. Chem., Int. Ed.*, 2009, **48**, 500–503.

29 Z. H. Xiang, C. Q. Fang, S. H. Leng and D. P. Cao, *J. Mater. Chem. A*, 2014, **2**, 7662–7665.

30 D. K. Singha and P. Mahata, *Inorg. Chem.*, 2015, **54**, 6373–6379.

31 S. Maruyama, K. Kikuchi, T. Hirano, Y. Urano and T. Nagano, *J. Am. Chem. Soc.*, 2002, **124**, 10650–10651.

32 X. Peng, J. Du, J. Fan, J. Wang, Y. Wu, J. Zhao, S. Sun and T. Xu, *J. Am. Chem. Soc.*, 2007, **129**, 1500–1501.

33 *SAINT, Program for Data Extraction and Reduction*, Bruker AXS, Inc, Madison, WI, 2001.

34 G. M. Sheldrick, *SADABS, Program for Empirical Adsorption Correction of Area Detector Data*, University of Göttingen, Germany, 2003.

35 G. M. Sheldrick, *SHELXS-2014, Program for the Crystal Structure Solution*, University of Göttingen, Germany, 2014.

36 G. M. Sheldrick, *SHELXL-2014, Program for the Crystal Structure refinement*, University of Göttingen, Germany, 2014.

37 P. van der Sluis and A. L. Spek, BYPASS: an effective method for the refinement of crystal structures containing disordered solvent regions, *Acta Crystallogr., Sect. A: Found. Crystallogr.*, 1990, **46**, 194–201.

38 A. L. Spek, PLATON, A Multipurpose Crystallographic Tool; Utrecht University: The Netherlands, 2005 or. A. L. Spek, Single Crystal Structure Validation with the Program PLATON, *J. Appl. Crystallogr.*, 2003, **36**, 7–13.

39 Q. Liu, L. N. Jin and W. Y. Sun, *Chem. Commun.*, 2012, **48**, 8814–8816.

40 J. Zhang, J. T. Bu, S. M. Chen, T. Wu, S. T. Zheng, Y. G. Chen, R. A. Nieto, P. Y. Feng and X. H. Bu, *Angew. Chem., Int. Ed.*, 2010, **49**, 8876–8879.

41 Y. Deng, Z. Y. Yao, P. Wang, Y. Zhao, Y. S. Kang and W. Y. Sun, *Sens. Actuators, B*, 2017, **244**, 114–123.

42 V. W. W. Yam and K. K. W. Lo, *Chem. Soc. Rev.*, 1999, **28**, 323–334.

43 M. D. Allendorf, C. A. Bauer, R. K. Bhakta and R. J. T. Houka, *Chem. Soc. Rev.*, 2009, **38**, 1330–1352.

44 D. Maspoch, D. Ruiz-Molina and J. Veciana, *Chem. Soc. Rev.*, 2007, **36**, 770–818.

45 G. De Santis, L. Fabbrizzi, M. Licchelli, A. Poggi and A. Taglietti, *Angew. Chem., Int. Ed. Engl.*, 1996, **35**, 202–204.

46 J. C. Dai, X. T. Wu, Z. Y. Fu, C. P. Cui, S. M. Hu, W. X. Du, L. M. Wu, H. H. Zhang and R. Q. Sun, *Inorg. Chem.*, 2002, **41**, 1391–1396.

47 N. B. Shustova, T. C. Ong, A. F. Cozzolino, V. K. Michaelis, R. G. Griffin and M. Dincă, *J. Am. Chem. Soc.*, 2012, **134**, 15061–15070.

48 H. J. Zhang, R. Q. Fan, W. Chen, J. Z. Fan, Y. W. Dong, Y. Song, X. Du, P. Wang and Y. L. Yang, *Cryst. Growth Des.*, 2016, **16**, 5429–5440.

49 S. S. Nagarkar, A. V. Desai and S. K. Ghosh, *Chem. Commun.*, 2014, **50**, 8915–8918.

50 Y. Ooyama, A. Matsugasako, K. Oka, T. Nagano, M. Sumomogi, K. Komaguchi, I. Imae and Y. Harima, *Chem. Commun.*, 2011, **47**, 4448–4450.

51 Q. Deng, Y. Li, J. Wu, Y. Liu, G. Fang, S. Wang and Y. Zhang, *Chem. Commun.*, 2012, **48**, 3009–3011.

52 S. G. Chen, Z. Z. Shi, L. Qin, H. L. Jia and H. G Zheng, *Cryst. Growth Des.*, 2017, **17**, 67–72.

53 B. Wang, X. L. Lv, D. W. Feng, L. H. Xie, J. Zhang, M. Li, Y. B. Xie, J. R. Li and H. C. Zhou, *J. Am. Chem. Soc.*, 2016, **138**, 6204–6216.

54 W. Sun, J. Wang, G. Zhang and Z. Liu, *RSC Adv.*, 2014, **4**, 55252–55255.

55 F. Yi, J. Li, D. Wu and Z. Sun, *Chem.–Eur. J.*, 2015, **21**, 11475–11482.

56 J. Chen, F. Yi, H. Yu, S. Jiao, G. Pang and Z. Sun, *Chem. Commun.*, 2014, **50**, 10506–10509.

57 S. S. Nagarkar, A. V. Desai and S. K. Ghosh, *Chem. Commun.*, 2014, **50**, 8915–8918.

58 S. J. Toal and W. C. Trogler, *J. Mater. Chem.*, 2006, **16**, 2871–2883.

59 S. S. Nagarkar, B. Joarder, A. K. Chaudhari, S. Mukherjee and S. K. Ghosh, *Angew. Chem., Int. Ed.*, 2013, **52**, 2881–2885.